NANO LETTERS

pubs.acs.org/NanoLett Letter

Interfacial Reaction and Diffusion at the One-Dimensional Interface of Two-Dimensional $PtSe_2$

Pawan Kumar, Andrew C. Meng, Kiyoung Jo, Eric A. Stach,* and Deep Jariwala*

Cite This: *Nano Lett.* 2022, 22, 4733−4740 Read Online

ACCESS | Metrics & More | Article Recommendations | Supporting Information

ABSTRACT: Two-dimensional (2D) $PtSe_2$ has potential applications in near-infrared optoelectronics because its band gap can be tuned by varying the layer thickness. There are several different platinum−selenide phases with different stoichiometries that result from high-temperature processing. In this report, we use *in situ* scanning/transmission electron microscopy (STEM) to investigate high-temperature phase transitions in 2D $PtSe_2$ and observe interfacial reactions as well as the Kirkendall effect. The 2D nature of $PtSe_2$ plays a key role in the unique one-dimensional interfaces that result during the formation of Se-poor phases (PtSe and $PtSe_{1-x}$) at the edges of the $PtSe_2$ crystals. The activation energy extracted for this formation suggests that the process is mediated by Se vacancies, as evidenced by the large strain variations in the material made via 4D STEM measurements. The observation of the Kirkendall effect in a 2D material suggests routes to engineer 1D edge chemistry for contact engineering in device applications.

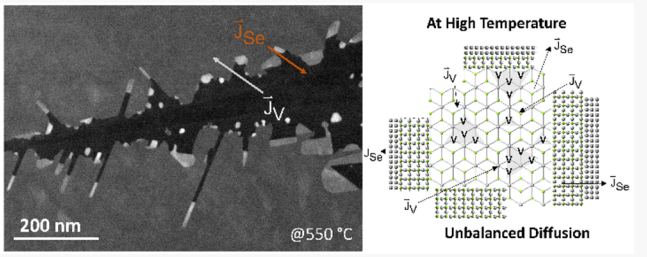

KEYWORDS: *Two-dimensional $PtSe_2$, Phase transformation, Se-vacancy, In situ TEM, 4D STEM*

Significant advances in the synthesis and processing of 2D materials have improved control over optoelectronic properties, enabling a wide-range of device applications.[1−4] Furthermore, recent device integration of 2D materials with both 1D nanowires and 3D bulk materials has highlighted the need to better understand effects arising from the dimensionality of their interfaces.[5−7] Different optoelectronic properties at these interfaces present opportunities for the creation of novel devices.[8] $PtSe_2$ is a noble-metal chalcogenide that can be either semiconducting (∼1.1 eV, single-layer), semimetallic (if few-layer), or metallic (if thick).[9,10] For materials with a bandgap in this range, the ability to tune band structure is highly desirable for the realization of optoelectronics in the near-infrared range for telecommunication applications.[2,11] $PtSe_2$ is also a promising material in microelectronics for enabling multifunctional devices that are 3D integrated on Silicon microprocessors due to the relatively low growth and processing temperatures (∼400 C) via vapor phase techniques.[9,10,12] These temperatures are compatible with back end of line (BEOL) integration in Si CMOS processing. In this study, we observe the formation of different Pt−Se phases *in situ* during high-temperature processing of $PtSe_2$ and focus on the role interfaces play in the mechanism of their formation. Our observations of the Kirkendall effect in a 2D chalcogenide system opens new opportunities of phase engineering as well as 1D interface engineering in a 2D layer for discovery of new physical phenomena and device applications such as contact engineering.

Diffusion-mediated phase transitions and kinetics of two-dimensional chalcogenides such as $PtSe_2$ are broadly understood, where the presence of stable intermediates with a higher metal to chalcogen ratio such as PtSe play a role in the dynamics of the transformation process.[13] The interplay between atomic-scale diffusivity and phase stabilization control the phases that are formed and the underlying microscopic mechanisms. PtSe formation from $PtSe_2$ occurs through lateral digestion and vertical growth, whereas Pd_2Se_3 formation from $PdSe_2$ occurs through vertical fusion.[14,15] The phase transitions in the Pt−Se system are temperature driven, and the crystal structure changes rapidly as the temperature approaches the phase change temperature of the 2D layers.[13,16] This is the primary hurdle in terms of commercial scaling for more exotic 2D materials such as noble metal chalcogenides.

Here, we study the kinetics of temperature-dependent phase transformations of $PtSe_2$ *in situ* in the transmission electron microscope (TEM) and *ex situ* using atomic force microscopy (AFM) and Raman spectroscopy. The *in situ* experiments involved resistive nonequilibrium heating of 2D $PtSe_2$ materials ranging from few layers thick to approximately 10 nm in thickness, and an ultrafast detection camera is used to capture the interfacial reaction kinetics of the $PtSe_2$ to $PtSe_{1-x}$ transformation. Our experiments are unique not just because

Received: March 3, 2022
Revised: June 3, 2022
Published: June 8, 2022

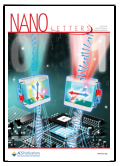

https://doi.org/10.1021/acs.nanolett.2c00874
Nano Lett. 2022, 22, 4733−4740

Scheme 1. Schematic of How Temperature Induced Changes in Vacancy Concentration and Diffusion Coefficient Result in Diffusional Phase Transformations

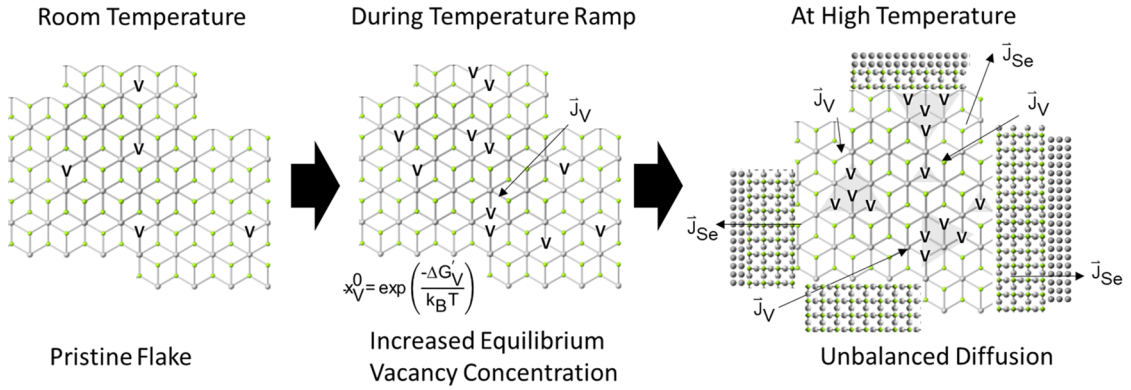

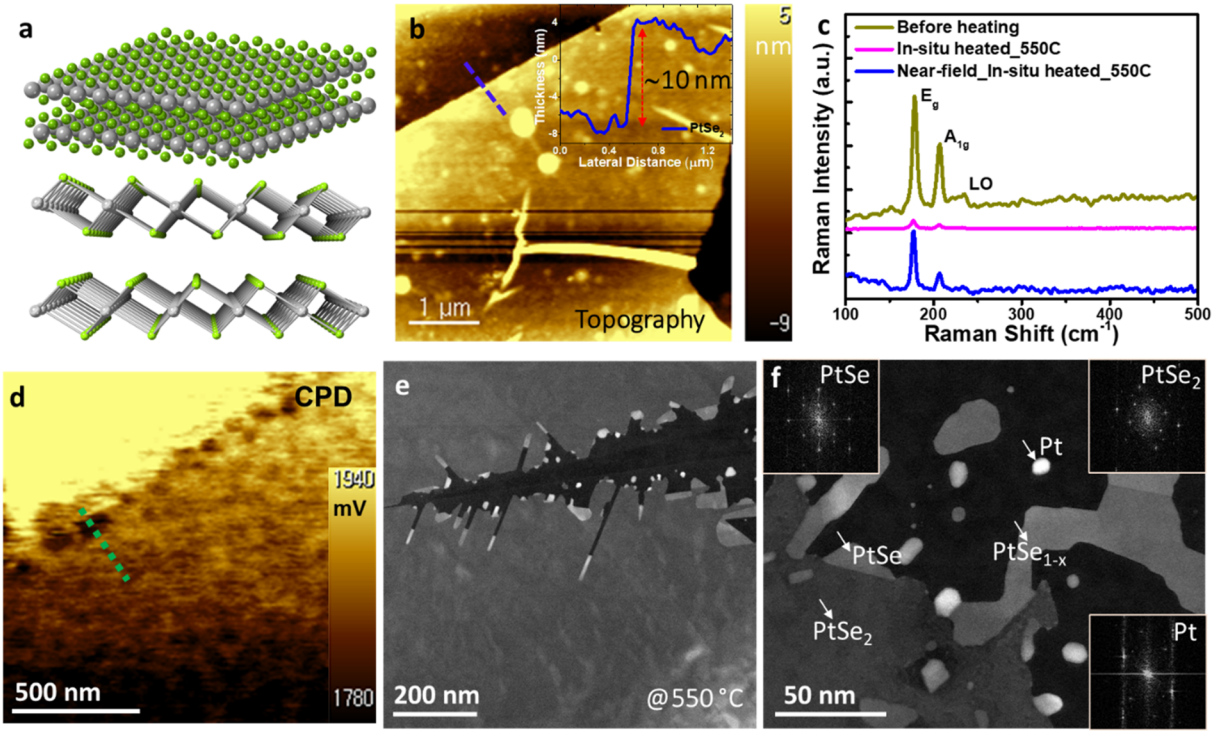

Figure 1. (a) Schematic model of the van der Waals $PtSe_2$ layers shown in top and side view. (b) AFM topography image of $PtSe_2$ that is a few layers thick. The inset shows the height profile. (c) Raman spectra comparing the as-prepared sample (green), the sample after *in situ* heating to 550 °C (pink), along-with near-field tip-enhanced Raman spectra (blue) which was also measured to confirm the characteristic features of $PtSe_2$. (d) Contact potential difference (CPD) map of the transformed phase of $PtSe_2$ located at the edge regions. (e) HAADF image after annealing few-layer $PtSe_2$ that had been heated to 550 °C and corresponding (f) formation of PtSe and $PtSe_{1-x}$ phases (labeled) along with FFTs from each phase, presented as insets.

of the *in situ* nature of the study but also because the rate of heating in our study is extremely high (>40 C/sec). This results in vapor pressures, strains, and defect concentrations in samples that are far away from those achieved via slow equilibrium heating in a furnace leading to formation of substoichiometric phases such as $PtSe_{1-x}$ and other phases such as PtSe that are not observed in equilibrium phase diagram of Pt−Se system.[17] A key observation was that the phase transformation process occurs rapidly at the edge of the 2D layer, which is a 1D boundary, and that vacancies appeared to be involved. Because the interface of a 2D material is 1D, this situation schematically resembles a combination of an interfacial reaction and the Kirkendall effect, except with unique pathways due to the dimensional confinement. The Kirkendall effect involves imbalanced diffusion arising from different chemical diffusivities of two components in a diffusion couple and can be accompanied by interfacial reactions that further contribute to the driving force through a chemical potential gradient. Applying this effect to 3D nanostructures has enabled the synthesis of various hollow core−shell structures.[18,19] The thermolysis of 2D $PtSe_2$ flakes results in the formation of Se-poor phases with lower Se chemical potential starting at the outer edges. This chemical potential gradient drives faster diffusion of Se from the flake to vacuum and results in the formation of Kirkendall voids in the flake. Heating the sample increases both the vacancy concentration and the diffusion coefficient, resulting in the observed phase transformations (Scheme 1). The interfacial

https://doi.org/10.1021/acs.nanolett.2c00874
Nano Lett. 2022, 22, 4733−4740

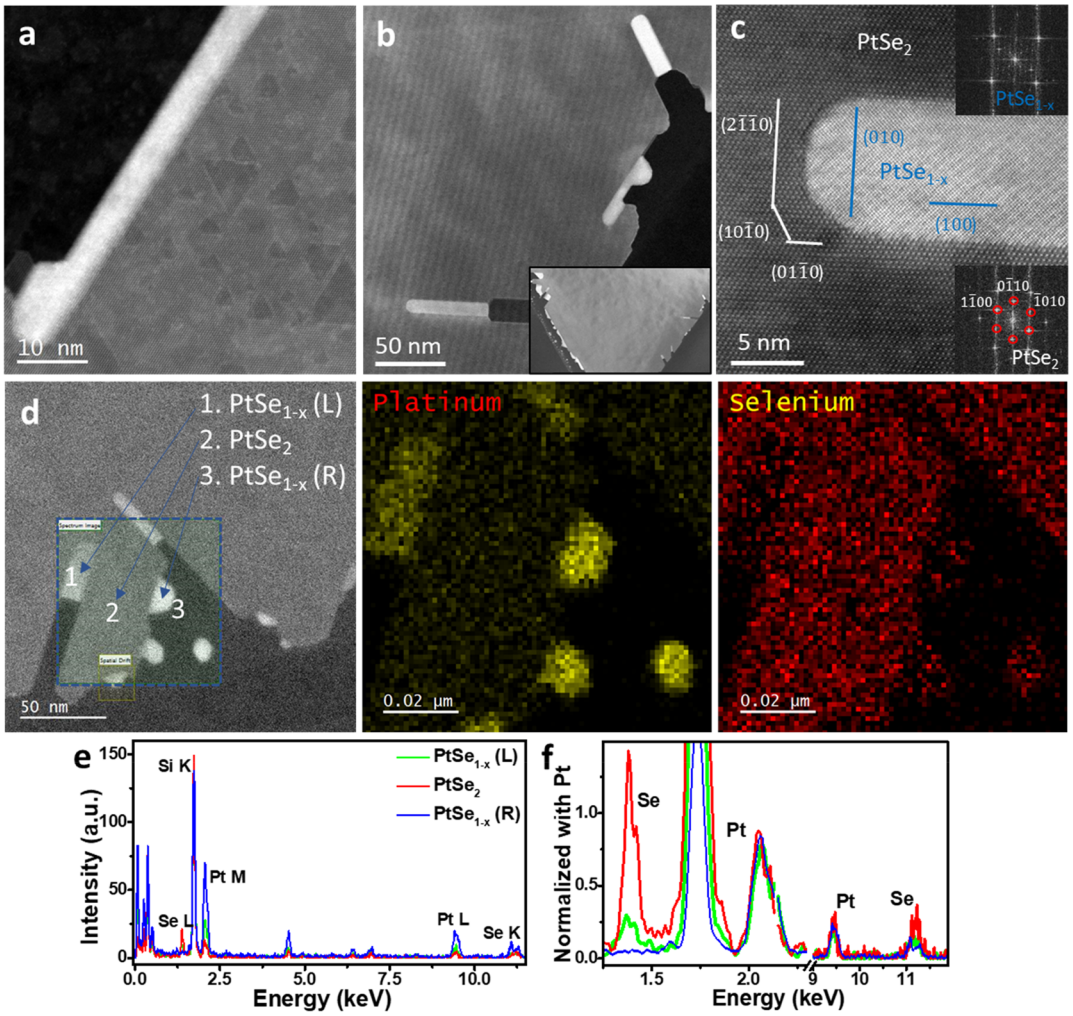

Figure 2. Diffusion at 1D interfaces and different rate of transformations of the 2D layer of $PtSe_2$ based upon the stoichiometry of $PtSe_{1-x}$. (a) Low magnification STEM image shows that the edges of $PtSe_2$ undergoes a phase transformation when heated to 550 °C. The transformed phases are the brighter regions. (b) STEM image of anisotropically transformed $PtSe_{1-x}$ regions and a low-magnification view (in inset image). (c) Atomically resolved interfaces of the two different phases of $PtSe_2$ with different crystallographic planes labeled, along with corresponding FFT diffractograms, inset. (d) Energy dispersive X-ray spectroscopic (EDS) elemental maps performed on the region that contains three different phases, which corroborates the different ratio of Se with respect to the Pt, as shown further in panel e. Panel f is a magnified view of a region of the spectra, after normalizing the intensity with respect to Pt for comparative visualization.

dynamics are completely captured by *in situ* TEM because the entire material system is electron transparent. By combining *in situ* and *ex situ* structural characterization, we gain important insight regarding the temperature-driven $PtSe_2$ phase transformations. These include the activation energy of the process, the stoichiometry of the chemical intermediates and products (PtSe, $PtSe_{1-x}$, and Pt), the dependence of the process on crystallographic orientation. We also characterize the spatial distribution of strain in the layers, which in turn provides indirect information regarding the vacancy concentration.

Understanding the atomic-scale structural characteristics of 2D materials is important to enable their manipulation in functional device applications. We have studied the atomistic transformation of 2D $PtSe_2$ layers at the atomic scale utilizing *in situ* vacuum heating inside the TEM. Figure 1a presents atomic models (perspective view, as well as side view) which highlight the van der Waals interactions in this layered material. We have used mechanically exfoliated, (see Experimental Section) few-layer $PtSe_2$ that was dry transferred to a microfabricated heating chip (see Figure S1). The corresponding height profile is shown in Figure 1b in the AFM (atomic force microscope) topographical image. Nonequilibrium vacuum heating was performed by resistively heating the embedded heating element in the microfabricated chip (see Experimental Section). Temperature is measured with the on-chip thermocouple and compared with IR spectroscopic measurements. Figure 1c presents the characteristic Raman spectra of the $PtSe_2$ flakes before and after heating to 550 °C (see Figure S2, bright-field TEM image before and after heating). We observed a significant intensity reduction of the characteristic Raman peaks of $PtSe_2$ after heating. The intensity reduction could be consistent with a change in symmetry of the phonon modes due to differences in the crystal structure of the transformed PtSe or $PtSe_{1-x}$[13] (see composition measurements, *vide infra*) and a decrease in the volume fraction of $PtSe_2$. To confirm whether the phonon modes changed due to a change in the crystal symmetry, we used near-field, tip-enhanced Raman spectroscopy (TERS). TERS from the same area of the transformed PtSe or $PtSe_{1-x}$ layer (Figure 1c) shows the exact same characteristic Raman peaks (positions of

https://doi.org/10.1021/acs.nanolett.2c00874
Nano Lett. 2022, 22, 4733−4740

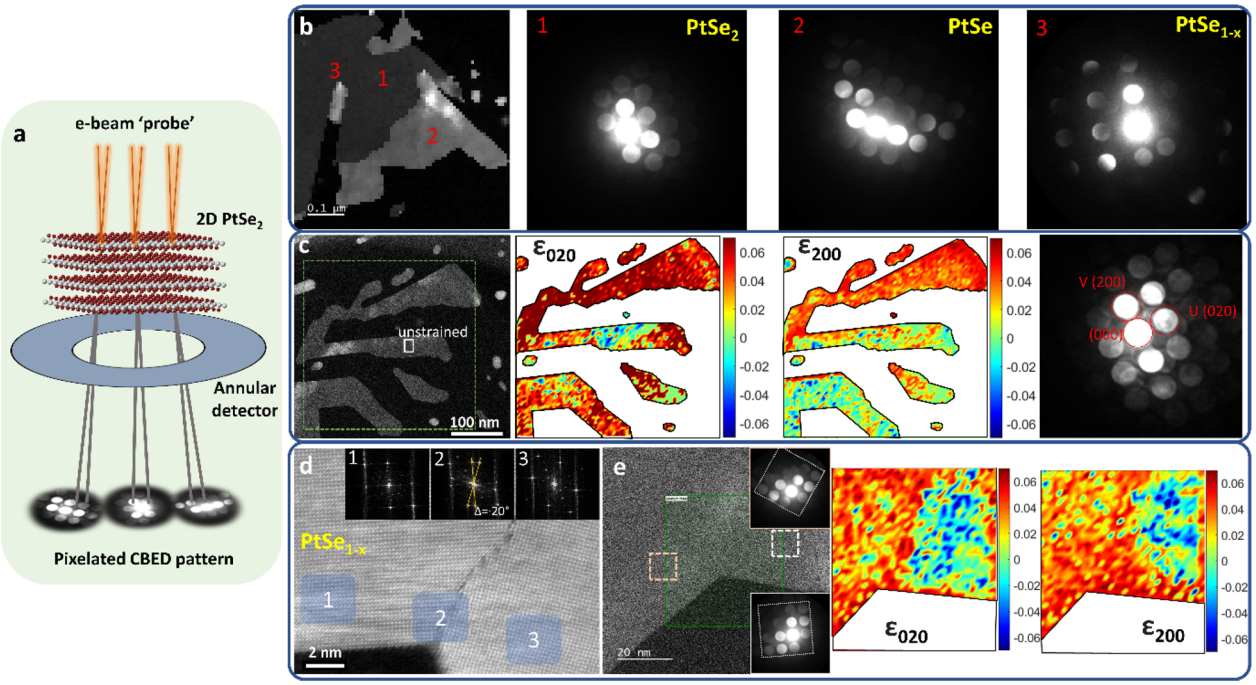

Figure 3. (a) Schematic of the 4D-STEM measurement from 2D $PtSe_2$. (b) STEM image with CBED patterns from all the three different phases ($PtSe_2$, PtSe and $PtSe_{1-x}$) after thermolysis at 550 °C. (c) A 4D-STEM strain map in the transformed cubic $PtSe_{1-x}$ region showing a large variation in both (020) and (200) components of strain. (d) Atomic scale HAADF-STEM image shows a low angle tilt boundary with FFT patterns from the marked regions 1−3, and the corresponding (e) 4D-STEM maps of (020) and (200) components of strain.

E_{2g} and A_{1g}) as are observed in bare $PtSe_2$. The TERS data suggests that the transformed PtSe or $PtSe_{1-x}$ layer exhibits similar phonon vibrational modes as in the $PtSe_2$ layer. Because of the lack of any experimental evidence in the literature about the Raman vibrational modes from PtSe or $PtSe_{1-x}$, it is difficult to make conclusive statements regarding the phonon interactions in these two materials; further examination, which is beyond the scope of the current work, would be required. We have also analyzed the work function, which is directly proportional to the contact potential difference (CPD) of the transformed phase using Kelvin probe force microscopy (KPFM). As shown in Figure 1d, the CPD map across the edge region of transformed $PtSe_2$ layer (also see Figure S3, which indicates the specific locations via TEM, topography, CPD mapped images and line profiles) shows a clear change in the work function across the transformed $PtSe_{1-x}$ phase as compared with the parent $PtSe_2$ layer.

Figure 1e presents a low magnification, high-angle annular dark field (HAADF) STEM image collected after heating to 550 °C. The contrast in the image shows brighter, higher atomic number domains at the outer edges, consistent with the presence of Se-poor regions, suggesting that thermolysis and phase transformations begin at the outer edges or cracks in the 2D layer of $PtSe_2$ (see Figure S4). Individual phases have been identified and are denoted with corresponding fast Fourier transformation (FFT) diffractograms (insets) in Figure 1f (see Figure S5). Conversion of the van der Waals layered structure of $PtSe_2$ to nonlayered, cubic-like phases (PtSe, $PtSe_{1-x}$), as well as complete transformation to Pt particles have also been observed (see Figures S6−S8).

Figure 2a shows the post-transformation structural characteristics of the material. There are three different stoichiometries observed: $PtSe_2$, PtSe, and $PtSe_{1-x}$. The Se-poor phases, which form from the loss of Se from $PtSe_2$, are observed to nucleate and grow at the edge of the $PtSe_2$ flake. The flake, which is initially uniform, is observed to develop triangular regions of darker contrast in the HAADF-STEM image. These darker regions in Figure 2a indicate decreased high-angle scattering that could be consistent with less material in the area due to triangular voids or vacancy clusters (see Figure S9). Finally, the symmetry of the Se-poor crystals is observed to differ from that of $PtSe_2$, as expected. To rationalize these observations, we consider that the activation energy for sulfur vacancy diffusion[20] in MoS_2 is expected to be lower than that of molybdenum vacancies.[21] This would result in a higher diffusion coefficient for the chalcogen compared to refractory metal atoms, especially at higher temperatures. Assuming the chalcogen (Se) vacancies diffuse faster than those of the noble metal (Pt) and combined with the knowledge that $PtSe_2$ decomposes into Se-poor phases upon heating,[13] we conjecture that the observed structural changes are due to more rapid Se diffusion to the surface, where the decomposition reaction occurs. As the diffusion of Se and Pt is not in balance, the build-up of vacancies in the $PtSe_2$ is consistent with the Kirkendall Effect. Conventionally, a hollow metal chalcogenide nanocrystal can be obtained via the Kirkendall Effect reacting a metal nanoparticle with a chalcogen;[22] the resulting diffusion across the 2D interface of the 3D material is imbalanced. Our observation of the $PtSe_2$ structural changes are analogous, except that the material is 2D and the interface is 1D. To rationalize the formation of Pt, we consider that depletion of Se from the sample due to continual flux of Se atoms from $PtSe_2$ to the edge surfaces and into vacuum would eventually form Pt. As the vapor pressure of Se is 1 Pa at 227 °C (100 kPa at 685 °C),[23] any Se atom flux reaching the sample edge surface would be expected to vaporize under $\sim 3 \times 10^{-5}$ Pa vacuum in the TEM column. The Pt nanoparticle in Figure 1f is completely disconnected

https://doi.org/10.1021/acs.nanolett.2c00874
Nano Lett. 2022, 22, 4733−4740

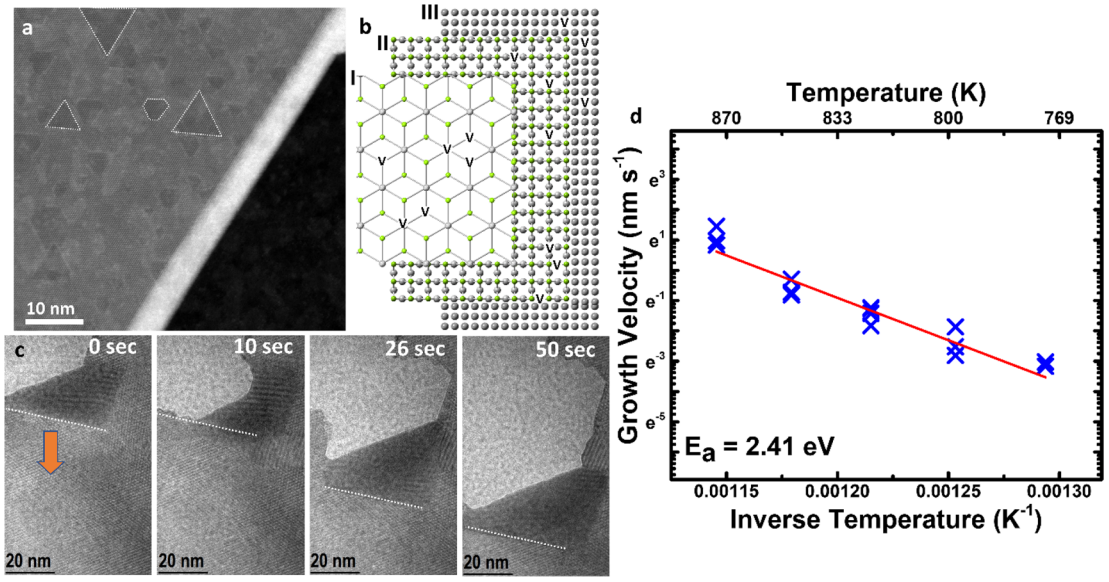

Figure 4. (a) HAADF-STEM image of a region where both imbalanced diffusion and interfacial reactions occur. (b) schematic depiction of three regions with different stoichiometries. Region I, hexagonal $PtSe_2$; Region II, cubic $PtSe_{1-x}$; Region III, metallic Pt. (c) TEM image sequence during heating at 550 C showing the growth of the transformed phase (indicated by the arrow) and corresponding (d) activation energy for the phase transformation from $PtSe_2$ to $PtSe_{1-x}$ as measured from the images in (c), and from Figures S13, S14 and *in situ* Videos S1, S2, and S3.

from the original flake, consistent with it having completely depleted its source of Se.

The HAADF STEM image shown in Figure 2b shows that the transformation from $PtSe_2$ to $PtSe_{1-x}$ occurs more rapidly in some regions of the sample and exhibits anisotropy. As the Se-poor domains that form are faceted, the anisotropic transformation shows that the growth rate of $PtSe_{1-x}$ depends on crystallographic orientation. Figure 2b inset is a lower magnification STEM image of the same region in Figure 2b. The region in Figure 2b is magnified to atomic resolution in Figure 2c, showing the atomic arrangement and the facets at the interface between $PtSe_2$ and $PtSe_{1-x}$. The white lines shown in Figure 2c correspond to the $[2\bar{1}\bar{1}0]$, $[10\bar{1}0]$, and $[01\bar{1}0]$ orientations of $PtSe_2$. The interface between the $PtSe_2$ and $PtSe_{1-x}$ is highly stepped, and there is an epitaxial relationship between the $PtSe_2$ and the $PtSe_{1-x}$, with $[01\bar{1}0]_{PtSe2}//[100]_{PtSe1-x}$ and $[2\bar{1}\bar{1}0]_{PtSe2}//[010]_{PtSe1-x}$. The micrographs show that the facets at the 1D interface between $PtSe_2$ and $PtSe_{1-x}$ have different lengths, consistent with the expected anisotropies in their interface energies. The first order diffraction spots of $PtSe_2$ have also been marked in the respective FFT pattern, shown as insets of Figure 2c (see Figure S10). The Se-poor $PtSe_{1-x}$ domain that has formed has a rectangular shape (see the bright contrast extending inward to 2D $PtSe_2$ layer). We have further examined the elemental compositional of the three different phases. Figure 2d presents energy dispersive X-ray spectroscopy (EDS) maps for the selected nanoscale region, which includes the $PtSe_2$ and $PtSe_{1-x}$ phases. The Pt and Se elemental maps show regions with three different levels of stoichiometries which further visualized by spectral intensity plot shown in Figure 2e. By normalizing the EDS spectra intensities with respect to the Pt, we find that regions 1 and 3 are consistent with $PtSe_{1-x}$ and that region 2 is consistent with $PtSe_2$. Figure 2f shows a comparison of normalized spectra for these three regions, indicated by 1 ($PtSe_{1-x}$ L), 2 ($PtSe_2$) and 3 ($PtSe_{1-x}$ R) phases. We can clearly observe the Pt to Se ratio is significantly reduced in the two regions, consistent with the formation of $PtSe_{1-x}$. We attribute these results to a possible dependence of the stoichiometry of the transformed $PtSe_{1-x}$ phase on the different 1D interfaces and Se vacancy-based reaction kinetics (see Figure S11).

Figure 3 shows 4D-STEM[24] maps of transformed and untransformed regions of $PtSe_2$. Convergent beam electron diffraction (CBED) patterns are collected as a function of spatial position, allowing crystallographic orientation and lattice constant to be obtained as a function of spatial position (Figure 3a). Post transformation, we observe that CBED patterns taken from regions with different contrast in the HAADF-STEM image have different lattice parameters and crystallographic symmetries, as expected based on the Pt to Se stoichiometry (Figure 3b). This directly detects the different phases through the diffraction patterns because $PtSe_2$ is hexagonal whereas the Se-deficient $PtSe_{1-x}$ and PtSe are observed to be cubic. Schematically, strain mapping in two component directions is obtained by measuring differences in the spacing between two diffracted beams with g-vectors perpendicular to each other and the transmitted beam in reciprocal space as a function of position. Thus, this only makes sense within a region in which the crystal symmetry is the same. Within a single cubic crystallographic domain, we map the strain distribution and find that the lattice parameter in the two in-plane directions varies significantly, on the order of a few percent. Since the sample stays relatively flat (Rq $\leq$ 1.25 nm, as measured in the AFM), physical undulation alone in the crystal is unlikely to result in this amount of strain variation. Instead, the lattice constant variation could be consistent with spatially varying selenium vacancy concentration.[25] Our post-transformation HR-STEM results also show contrast consistent with varying vacancy concentration, *vide infra*, Figure 4. Finally, we perform a strain map across a grain boundary between two cubic Se-poor domains imaged using aberration corrected STEM (Figure 3d and see Figure S12). These show an approximately 6% difference in the two in-plane lattice parameters (Figure 3e). The results suggest

https://doi.org/10.1021/acs.nanolett.2c00874
Nano Lett. 2022, 22, 4733−4740

that the formation of selenium poor phases at the edge of $PtSe_2$ is correlated with a local variation in the lattice parameter.

By performing an *in situ* heating experiments at different temperatures and observing the dependence of the growth rate of the Se-poor $PtSe_{1-x}$ phase, we can quantify the kinetics of the $PtSe_2$ transformation process. A schematic of the process by which Se vacancy diffusion drives the $PtSe_2$ phase change during heating is shown in Figure 4a,b. Imbalanced diffusion results in a vacancy flux into the $PtSe_2$ flake while regions of differing stoichiometry (Region I, hexagonal $PtSe_2$; Region II, cubic $PtSe_{1-x}$; Region III, metallic Pt) are formed due to interfacial reactions. To measure the growth rate, we examined the *in situ* TEM video data collected during heating and measured the velocity of the $PtSe_2/PtSe_{1-x}$ interface as shown in Figure 4c (also see Figure S13, S14 and *in situ* Videos S1, S2, and S3). After performing this experiment multiple times at temperatures ranging from 500 to 600 °C, we observe that the interface velocity exhibits an Arrhenius dependence on temperature (Figure 4d). The activation energy obtained by fitting the data is 2.41 eV. This is consistent with the expected diffusion barrier for Se in $PtSe_2$, which has been calculated to be approximately 2.56 eV.[26] Because the activation energy for diffusion of an isolated Se vacancy is higher (4.25 eV), our data is consistent with a material with a typical vacancy concentration where interaction of multiple vacancies lowers the activation energy.[27,28] This mechanism involving multiple vacancies also is consistent with the observation of dark triangular regions, which appear to be vacancy clusters or aggregates. While extrinsic contamination in 2D materials is well-known and could potentially impact the nucleation of substoichiometric Pt−Se species, we do not find significant spatial variation in extrinsic components in the EDS spectra in the fresh sample, and most of the extrinsic X-ray signal in the EDS spectra can be attributed to hole count (Figure S15).[29] Furthermore, the dominant variable affecting the temperature-induced phase transformations is the distance from the flake edge, consistent with a diffusional transformation (as opposed to nucleation and growth). The activation energy extracted from the *in situ* data is also consistent with this picture.

In summary, we have studied and analyzed the 1D interfacial kinetics and reactions that occur in 2D $PtSe_2$ layers at elevated temperatures. Ultrafast *in situ* heating of $PtSe_2$ has been performed utilizing a microfabricated heating chip coupled with analysis of the phase transformations and accompanying stoichiometric changes. Multiple Pt−Se phases with Se-poor stoichiometries are formed during $PtSe_2$ heating. PtSe, off-stoichiometric $PtSe_{1-x}$, and Pt are observed at the 1D interface of $PtSe_2$. The Se-poor regions are highly anisotropic, and within Se-poor $PtSe_{1-x}$ domains, there is significant variation in lattice strain consistent with large variations in vacancy concentration. Darker, triangular contrast in the dark field STEM images of $PtSe_2$ is also consistent with vacancies arising from imbalanced diffusion and the Kirkendall effect. We observe the kinetics of the phase transformation *in situ* in the TEM, and by extracting an activation energy, find that the mechanism is consistent with Se vacancy diffusion. Our observations of the Kirkendall effect in a Pt−Se systems suggests that with availability of multiple phases is a given 2D material system there is more room for tunability of the material for contact engineering in device applications. Another implication of this study from the basic science side is the discovery of new and metastable phases that are unknown and yet to be predicted with potentially novel properties such as $PtSe_{1-x}$ which has been observed for the first time. Finally, the 1D heterojunctions and interfaces occurring at the phase boundaries as reported in this study could potentially host interesting electronic states that have not been uncovered yet since the density of states and spin−orbit coupling can abruptly vary across the 1D interface.

EXPERIMENTAL SECTION

Materials Synthesis and Processing. Two-dimensional few-layer $PtSe_2$ flakes were obtained from the bulk single crystal $PtSe_2$ (purchased from hQ graphene, Netherland) using the Scotch tape method. Exfoliated few-layer $PtSe_2$ was transferred to prefabricated microfabricated heating chip (Hummingbird Scientific LLC) using dry transfer technique with help of thin PDMS stamp. After transferring to a chip, we utilized a forming gas-based annealing of the $PtSe_2$ flake up to 300 °C to remove all the residual PDMS contaminant over 2D layer, which was present after dry transfer process.

Surfaces and Spectroscopic Analysis. The thickness of the $PtSe_2$ layer was determined using atomic force microscopy height imaging (AFM, OmegaScope-R (AIST-NT) setup). Also, Kelvin-probe force microscopy (KPFM) measurement was accomplished with the above-mentioned AFM setup. A gold tip was used and biased by 3 V while the sample was grounded. Tip calibration was done with the help of a freshly cleaved highly oriented pyrolytic graphite (HOPG) sample. Spectroscopic signatures from the $PtSe_2$ were analyzed using Raman Spectroscopy (LabRAM HR Evolution -Horiba) utilizing 633 nm LASER. Near-field, tip-enhanced Raman spectroscopy was performed using the above-mentioned AFM system, which is attached and upgraded with the LabRam Horiba Raman spectroscopy system. Au-coated OMNI-TERS probes (APP Nano) were used for the measurement of tip-enhanced Raman spectrum.

Structural and Strain Analysis. TEM characterization and 4D-STEM strain mapping were performed using a JEOL JEM-F200, and aberration corrected (probe) STEM characterization was performed using a JEOL NEOARM. The 4D-STEM data were collected using STEMx (Gatan) with a Gatan OneView camera (4k × 4k) on the F200. Diffraction patterns were acquired for 0.04 s, and drift correction was performed for each row.

ASSOCIATED CONTENT

Supporting Information

The Supporting Information is available free of charge at https://pubs.acs.org/doi/10.1021/acs.nanolett.2c00874.

Optical micrograph of TEM chip, additional characterization of the exfoliated $PtSe_2$ crystals via AFM, KPFM, HAADF STEM, and EDS mapping in TEM including visualization of atomically resolved phase transitions with their descriptions (PDF)

Video (S1) of TEM image sequence during heating at 600 C showing the growth of the transformed phase and corresponding activation energy calculated for the phase transformation from $PtSe_2$ to $PtSe_{1-x}$ (MP4)

Video (S2) of TEM image sequence during heating at 600 C showing the anisotropic growth of the transformed phase and corresponding activation energy calculated for the phase transformation from $PtSe_2$ to $PtSe_{1-x}$ (MP4)

https://doi.org/10.1021/acs.nanolett.2c00874
Nano Lett. 2022, 22, 4733−4740

Video (S3) of TEM image sequence after heating and staying at 500 C showing the anisotropic growth of the transformed phase from $PtSe_2$ to $PtSe_{1-x}$ (MP4)

AUTHOR INFORMATION

Corresponding Authors

Eric A. Stach − *Department of Materials Science and Engineering, University of Pennsylvania, Philadelphia, Pennsylvania 19104, United States;* orcid.org/0000-0002-3366-2153; Email: dmj@seas.upenn.edu

Deep Jariwala − *Department of Electrical and Systems Engineering, University of Pennsylvania, Philadelphia, Pennsylvania 19104, United States;* orcid.org/0000-0002-3570-8768; Email: stach@seas.upenn.edu

Authors

Pawan Kumar − *Department of Electrical and Systems Engineering, University of Pennsylvania, Philadelphia, Pennsylvania 19104, United States; Department of Materials Science and Engineering, University of Pennsylvania, Philadelphia, Pennsylvania 19104, United States;* orcid.org/0000-0002-5764-2915

Andrew C. Meng − *Department of Materials Science and Engineering, University of Pennsylvania, Philadelphia, Pennsylvania 19104, United States;* orcid.org/0000-0002-3060-8928

Kiyoung Jo − *Department of Electrical and Systems Engineering, University of Pennsylvania, Philadelphia, Pennsylvania 19104, United States;* orcid.org/0000-0003-4587-234X

Complete contact information is available at: https://pubs.acs.org/10.1021/acs.nanolett.2c00874

Author Contributions

P.K., E.A.S., and D.J. conceived and planned the project; P.K. prepared all the samples and performed *in situ* heating, microscopy imaging, and spectroscopy (Raman and EDS) experiments; P.K. and A.C.M. completed 4D-STEM imaging; A.C.M. plotted the strain map using MATLAB code and help to analyze the images for the activation energy calculation; K.J. performed the AFM and KPFM measurements and further analysis of the images. P.K., A.C.M., E.A.S., and D.J. wrote the whole manuscript with the contribution of K.J.

Notes

The authors declare the following competing financial interest(s): Eric Stach has an equity interest in Hummingbird Scientific. Instrumentation from Hummingbird Scientific is used in this study.

ACKNOWLEDGMENTS

P.K., D.J., and E.A.S acknowledge primary support for this work from National Science Foundation (DMR-1905853) and partial support from the University of Pennsylvania Materials Research Science and Engineering Center (MRSEC) (DMR-1720530), in addition to usage of MRSEC supported facilities. A.C.M. acknowledges support from the BASF Corporation. The sample fabrication, assembly, and characterization were carried out at the Singh Center for Nanotechnology at the University of Pennsylvania, supported by the National Science Foundation (NSF) National Nanotechnology Coordinated Infrastructure Program Grant NNCI-1542153. K.J. was supported by the Vagelos Institute of Energy Science and Technology Graduate Fellowship.

REFERENCES

(1) Jariwala, D.; Sangwan, V. K.; Lauhon, L. J.; Marks, T. J.; Hersam, M. C. *ACS Nano* **2014**, *8* (2), 1102−1120.

(2) Yu, X.; Yu, P.; Wu, D.; Singh, B.; Zeng, Q.; Lin, H.; Zhou, W.; Lin, J.; Suenaga, K.; Liu, Z.; Wang, Q. J. *Nat. Commun.* **2018**, *9* (1), 1545.

(3) Kumar, P.; Zhu, K.; Gao, X.; Wang, S.-D.; Lanza, M.; Thakur, C. S. *npj 2D Materials and Applications* **2022**, *6* (1), 8.

(4) Ribeiro, M.; Gentile, G.; Marty, A.; Dosenovic, D.; Okuno, H.; Vergnaud, C.; Jacquot, J.-F.; Jalabert, D.; Longo, D.; Ohresser, P.; Hallal, A.; Chshiev, M.; Boulle, O.; Bonell, F.; Jamet, M. *npj 2D Materials and Applications* **2022**, *6* (1), 10.

(5) Bae, S.-H.; Kum, H.; Kong, W.; Kim, Y.; Choi, C.; Lee, B.; Lin, P.; Park, Y.; Kim, J. *Nat. Mater.* **2019**, *18* (6), 550−560.

(6) Liu, Y.; Coppens, M.-O.; Jiang, Z. *Chem. Soc. Rev.* **2021**, *50* (21), 11747−11765.

(7) Jariwala, D.; Sangwan, V. K.; Wu, C.-C.; Prabhumirashi, P. L.; Geier, M. L.; Marks, T. J.; Lauhon, L. J.; Hersam, M. C. *Proc. Natl. Acad. Sci. U. S. A.* **2013**, *110* (45), 18076−18080.

(8) Kumar, P.; Lynch, J.; Song, B.; Ling, H.; Barrera, F.; Kisslinger, K.; Zhang, H.; Anantharaman, S. B.; Digani, J.; Zhu, H.; Choudhury, T. H.; McAleese, C.; Wang, X.; Conran, B. R.; Whear, O.; Motala, M. J.; Snure, M.; Muratore, C.; Redwing, J. M.; Glavin, N. R.; Stach, E. A.; Davoyan, A. R.; Jariwala, D. *Nat. Nanotechnol.* **2022**, *17* (2), 182−189.

(9) Ansari, L.; Monaghan, S.; McEvoy, N.; Coileáin, C. Ó.; Cullen, C. P.; Lin, J.; Siris, R.; Stimpel-Lindner, T.; Burke, K. F.; Mirabelli, G.; Duffy, R.; Caruso, E.; Nagle, R. E.; Duesberg, G. S.; Hurley, P. K.; Gity, F. *npj 2D Materials and Applications* **2019**, *3* (1), 33.

(10) Wang, Y.; Li, L.; Yao, W.; Song, S.; Sun, J. T.; Pan, J.; Ren, X.; Li, C.; Okunishi, E.; Wang, Y.-Q.; Wang, E.; Shao, Y.; Zhang, Y. Y.; Yang, H.-t.; Schwier, E. F.; Iwasawa, H.; Shimada, K.; Taniguchi, M.; Cheng, Z.; Zhou, S.; Du, S.; Pennycook, S. J.; Pantelides, S. T.; Gao, H.-J. *Nano Lett.* **2015**, *15* (6), 4013−4018.

(11) Wu, D.; Wang, Y.; Zeng, L.; Jia, C.; Wu, E.; Xu, T.; Shi, Z.; Tian, Y.; Li, X.; Tsang, Y. H. *ACS Photonics* **2018**, *5* (9), 3820−3827.

(12) Yim, C.; Passi, V.; Lemme, M. C.; Duesberg, G. S.; Ó Coileáin, C.; Pallecchi, E.; Fadil, D.; McEvoy, N. *npj 2D Materials and Applications* **2018**, *2* (1), 5.

(13) Ryu, G. H.; Chen, J.; Wen, Y.; Warner, J. H. *Chem. Mater.* **2019**, *31* (23), 9895−9903.

(14) Oyedele, A. D.; Yang, S.; Feng, T.; Haglund, A. V.; Gu, Y.; Puretzky, A. A.; Briggs, D.; Rouleau, C. M.; Chisholm, M. F.; Unocic, R. R.; Mandrus, D.; Meyer, H. M.; Pantelides, S. T.; Geohegan, D. B.; Xiao, K. *J. Am. Chem. Soc.* **2019**, *141* (22), 8928−8936.

(15) Ryu, G. H.; Zhu, T.; Chen, J.; Sinha, S.; Shautsova, V.; Grossman, J. C.; Warner, J. H. *Adv. Mater.* **2019**, *31* (46), 1904251.

(16) Ipser, K. W. R. a. H. *J. Phase Equilib.* **1994**, *15* (1), 6.

(17) Pt-Se Binary Phase Diagram 0−100 at. % Se: Datasheet from PAULING FILE Multinaries ed. − 2012. In *SpringerMaterials, Springer-Verlag Berlin Heidelberg & Material Phases Data System (MPDS)*; Switzerland & National Institute for Materials Science (NIMS), Japan, 2016.

(18) Jin fan, H.; Knez, M.; Scholz, R.; Nielsch, K.; Pippel, E.; Hesse, D.; Zacharias, M.; Gösele, U. *Nat. Mater.* **2006**, *5* (8), 627−631.

(19) Tu, K. N.; Gösele, U. *Appl. Phys. Lett.* **2005**, *86* (9), 093111.

(20) Le, D.; Rawal, T. B.; Rahman, T. S. *J. Phys. Chem. C* **2014**, *118* (10), 5346−5351.

(21) Hong, J.; Pan, Y.; Hu, Z.; Lv, D.; Jin, C.; Ji, W.; Yuan, J.; Zhang, Z. *Nano Lett.* **2017**, *17* (6), 3383−3390.

(22) Yin, Y.; Rioux, R. M.; Erdonmez, C. K.; Hughes, S.; Somorjai, G. A.; Alivisatos, A. P. *Science* **2004**, *304* (5671), 711−714.

(23) Lide, D. R. *CRC handbook of chemistry and physics*; CRC Press, 2004; Vol. *85*.

(24) Ophus, C. *Microscopy and Microanalysis* **2019**, *25* (3), 563−582.

https://doi.org/10.1021/acs.nanolett.2c00874
Nano Lett. 2022, 22, 4733−4740

(25) Gao, C.; Yang, X.; Jiang, M.; Chen, L.; Chen, Z.; Singh, C. V. *Phys. Chem. Chem. Phys.* **2021**, *23* (10), 6298−6308.
(26) Gao, J.; Cheng, Y.; Tian, T.; Hu, X.; Zeng, K.; Zhang, G.; Zhang, Y.-W. *ACS Omega* **2017**, *2* (12), 8640−8648.
(27) Interdiffusion and Kirkendall Effect. In *Diffusion in Solids: Fundamentals, Methods, Materials, Diffusion-Controlled Processes*; Springer Berlin Heidelberg: Berlin,, 2007; pp 161−177.
(28) Dependence of Diffusion on Temperature and Pressure. In *Diffusion in Solids: Fundamentals, Methods, Materials, Diffusion-Controlled Processes*; Springer Berlin Heidelberg: Berlin,, 2007; pp 127−149.
(29) Williams, D. B.; Carter, C. B. X-ray Spectra and Images. In *Transmission Electron Microscopy: A Textbook for Materials Science*; Springer: Boston, MA, 2009; pp 605−623.

https://doi.org/10.1021/acs.nanolett.2c00874
Nano Lett. 2022, 22, 4733−4740